JGR Earth Surface

RESEARCH ARTICLE
10.1029/2018JF004943

Surface Deformation and Influence of Hydrological Mass Over Himalaya and North India Revealed From a Decade of Continuous GPS and GRACE Observations

Ajish P. Saji[1], P. S. Sunil[1,2], K. M. Sreejith[3], Param K. Gautam[4], K. Vijay Kumar[1], M. Ponraj[1], S. Amirtharaj[1], Rose Mary Shaju[1,2], S. K. Begum[5], C. D. Reddy[1], and D. S. Ramesh[1]

[1]Indian Institute of Geomagnetism (DST), Mumbai, India, [2]Department of Marine Geology and Geophysics, Cochin University of Science and Technology (CUSAT), Kochi, India, [3]Geosciences Division, Space Applications Centre (ISRO), Ahmadabad, India, [4]Wadia Institute of Himalayan Geology (DST), Dehradun, India, [5]Department of Geophysics, Andhra University (AU), Visakhapatnam, India

Abstract The India-Eurasia collision, driven by tectonic forcing, is modulated by nontectonic forcing allied to seasonal variations in the neighboring regions. To decipher the ground deformation in response to hydrological mass variations of the Himalaya and North India, we analyzed continuous Global Positioning System (cGPS) observations from 50 sites together with Gravity Recovery and Climate Experiment (GRACE) data for the period 2004–2015. Vertical components of surface deformation derived from GPS and GRACE show moderate to high-level amplitude correlation with a slope value of 0.76 and a level of phase delay from ±25° to ±30°. The average weighted root-mean-square reduction (WRMS) of 17.72% suggests the prominence of hydrological mass variations particularly over the sub-Himalaya and Indo-Gangetic Plain (IGP). GPS-derived vertical deformation after correcting the hydrological effects utilizing GRACE observations suggests that the sub-Himalaya and IGP are undergoing subsidence and the surrounding areas show uplift. In addition to the tectonic and nontectonic forcings, an unsustainable consumption of groundwater associated to irrigation and other anthropogenic uses influence the subsidence rate in the IGP and sub-Himalaya. Further, 2-D elastic dislocation modeling suggests that GRACE correction to the GPS vertical velocity causes a reduction in the subsurface slip rate estimation over the Main Himalayan Thrust (MHT) system by 12.06% and improves the chi-square misfit by 20.32%.

Key Points:
- New cGPS and GRACE data reveal the prominence of previously unnoticed hydrological mass effects in sub-Himalaya and Indo-Gangetic Plain
- GRACE-reduced cGPS vertical deformation suggests that sub-Himalaya and IGP are undergoing subsidence and the surrounding areas show uplift
- In addition to tectonic and nontectonic forcings, unsustainable consumption of groundwater for anthropogenic usage influences the subsidence

Supporting Information:
- Supporting Information S1

Correspondence to:
P. S. Sunil,
sunilpsiig@gmail.com

Citation:
Saji, A. P., Sunil, P. S., Sreejith, K. M., Gautam, P. K., Kumar, K. V., Ponraj, M., et al. (2020). Surface deformation and influence of hydrological mass over Himalaya and North India revealed from a decade of continuous GPS and GRACE observations. *Journal of Geophysical Research: Earth Surface*, *125*, e2018JF004943. https://doi.org/10.1029/2018JF004943

Received 7 NOV 2018
Accepted 9 DEC 2019
Accepted article online 3 JAN 2020

1. Introduction

The ongoing underthrusting of the Indian plate below the Tibetan Plateau along the Main Himalayan Thrust (MHT) results in shortening of the Indian lithosphere mostly at the Main Frontal Thrust (MFT), the Main Boundary Thrust (MBT), and the Main Central Thrust (MCT). This shortening causes uplift of the Tibetan Plateau (Molnar & Tapponnier, 1975). As a consequence of such a collision, the strain energy accumulated along the MHT is episodically released in the form of major (*Mw* 7.0–7.9) to great (*Mw* ≥ 8.0) destructive earthquakes in the Himalaya, Tibetan Plateau, and Indian subcontinent (Zhao et al., 2011). Among such earthquakes that occurred during the last century, the 1897 Shillong Plateau (*Mw* ~8.1), 1905 Kangra (*Mw* ~7.8), 1934 Nepal-Bihar (*Mw* 8.1), 1950 Assam (*Mw* 8.5), 2005 Kashmir (*Mw* 7.6), and 2015 Nepal (*Mw* 7.8) (Figure 1) are the notable ones. In particular, the 25 April 2015 Gorkha Nepal earthquake of magnitude *Mw* 7.8 and its presumed *Mw* 7.2 aftershock on 12 May 2015 necessitates a more detailed understanding of the tectonics and kinematics of the Indian plate (Bilham et al., 2017; Sreejith et al., 2016, 2018).

Understanding the surface deformation and slip rate during these earthquakes and their partitioning into seismic and aseismic components is the key factor to comprehend the convergence dynamics and attendant underthrusting of the Indian plate in this region. The slip rates across the MHT are derived on the basis of great earthquake magnitudes and geological evidence and the values lie between 8 and 21 mm/year (Lavé & Avouac, 2000; Molnar, 1990). Furthermore, the slip rates derived from the well-constrained geodetic observations are between 10 and 20 mm/year (Ader et al., 2012; Bilham et al., 1997; Jade et al., 2014; Sreejith et al., 2018). This agreement among slip rates inferred from geologic considerations and geodetic measurements confirms that the elastic strain accumulation in the Himalaya is high. The accumulated strain is subsequently released as seismic slip by way of earthquake occurrence or aseismic creeping where the strain

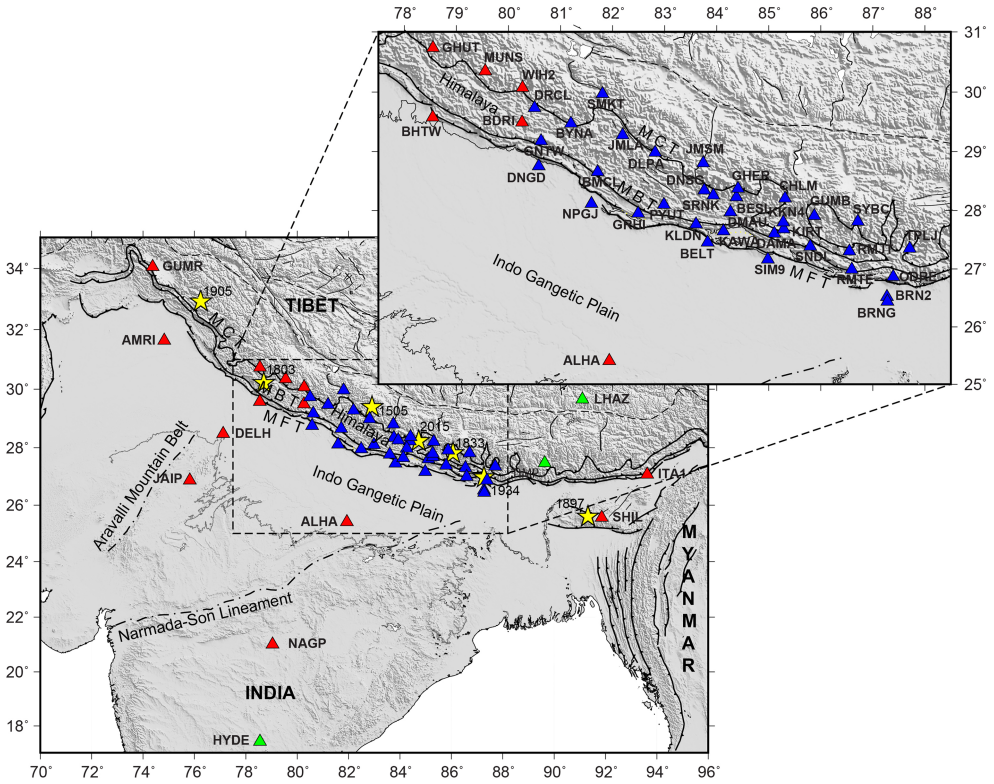

Figure 1. Tectonic map of study area with epicenter locations of large earthquakes in yellow stars. Continuous and dashed black lines depicts the major faults and lineaments respectively. The three major thrusts in the region, the MFT, MBT, and MCT, are shown. Red, blue, and green triangles represent the GPS sites belonging to networks of India, Nepal, and International GNSS Services (IGS), respectively.

accumulated zone is not locked. However, to accurately comprehend the tectonically induced slip rates, it is important to quantify the nontectonic factors that can influence the geodetic measurements.

In this context, it is pertinent to note that the time series recorded at continuous Global Positioning System (cGPS) stations in the Himalaya and neighboring regions are always affected by nontectonic seasonal effects, for example, ocean tidal loading (Agnew, 1997; Williams & Penna, 2011), atmospheric pressure loading (Tregoning & van Dam, 2005; van Dam et al., 1994), and terrestrial water storage influences (Bettinelli et al., 2008; Chanard et al., 2014; Fu & Freymueller, 2012), also referred to as nontectonic forces in the literature. The redistribution of these forces also deforms the Himalayan crust and modulates the GPS position time series.

Compared to ocean and atmospheric loading effects, the changes in the water storage and associated seasonal surface load variations produce more significant crustal deformation and are relatively difficult to quantify using global models. However, the launch of the Gravity Recovery and Climate Experiment (GRACE) satellite with its ability to measure the integrated Earth's gravity field in the form of spherical harmonic coefficients mitigated this difficulty to an extent. Combined use of GPS and GRACE is now commonly employed to quantify the variations of hydrologic mass. This combination facilitates the estimation of the direct influence of elastic crustal deformation and tectonic dynamic processes precisely (Tapley et al., 2004; Jin et al., 2013; Amos et al., 2014).

In the Himalaya, the influence of seasonal signals on the radial (vertical) component of GPS time series is strong and correlates well with the vertical signals from GRACE (Bettinelli et al., 2008; Chanard et al., 2014; Fu et al., 2012; Gautam et al., 2017). Similar observations are reported for the Tibetan Plateau and south India as well (He et al., 2018; Pan et al., 2018; Tiwari et al., 2014; Zou et al., 2015). In regions like the Himalaya, the seasonal water loading and unloading effect from glaciers as well as monsoon precipitation play a key role in the deformation and associated seismicity (Bettinelli et al., 2008; Kundu et al., 2015;

Johnson et al., 2017). Similarly, the neighboring Indo-Gangetic Plain (IGP), the major alluvial aquifer system in India, also deforms seasonally by the Himalayan river system and monsoon precipitation (Tiwari et al., 2009; Panda et al., 2018). Reports also suggest that the IGP deforms vertically due to the excessive extraction of groundwater for irrigation and other anthropogenic activities (Mishra et al., 1993; Rodell et al., 2009). However, recent geodetic studies have not carefully considered the effects of hydrologic mass variations over the IGP province and surroundings (Bettinelli et al., 2008; Fu & Freymueller, 2012; Pan et al., 2018).

In the present study, apart from the formerly used cGPS and GRACE data in different investigations (26 sites at Nepal Himalaya) (Bettinelli et al., 2008; Fu & Freymueller, 2012; Pan et al., 2018), we additionally used 24 more sites spread over NW and NE Himalayas and North Indian regions for a decade of observations starting in 2004. As we are mainly focused on delineating the contribution of hydrological mass variation factors over the study region in the absence of coseismic deformation, we restrict our data analysis prior to the 2015 *Mw* 7.6 Gorkha earthquake.

2. Data Analysis

2.1. GPS Network and Data

We used cGPS data from 2004–2015, acquired from 13 sites of the Indian Geodetic Network, 34 sites of the Nepal Geodetic Network, and 3 sites of the International Global Navigation Satellite System Service (IGS) Network. In order to achieve robust results with high precision, data from GPS sites in operation for more than three years are used in the analysis (e.g., Blewitt & Lavallée, 2002).

To obtain the time series for all GPS sites in ITRF2008 (Altamimi et al., 2011), we used the GAMIT/GLOBK 10.5 software from Massachusetts Institute of Technology (USA). The daily positions were estimated from 24-hr GPS dual-frequency phase and code observations in a two-step procedure (Herring, 2005; King & Bock, 2005). In the first step, satellite orbital parameters published by IGS were used and ionospheric effects were removed by means of the ionosphere-free linear combination. Further, Earth tidal and pole tidal effects were corrected following the International Earth Rotations Reference System (IERS2010) conventions, while ocean tidal loading effects were corrected using model Finite Element Solution (FES2012). The non-tidal ocean loading effect is eliminated using an ocean bottom pressure model with temporal and spatial resolution of 6 hr and 0.5°, respectively (van Dam et al., 2012). For tropospheric delay correction, to estimate the zenith delay and horizontal gradients, we have employed the Global Mapping Function using the Global Pressure Temperature model (Bohem et al., 2006). The atmospheric loading effects have been derived from the National Center for Environmental Protection (NCEP) reanalysis surface pressure data set, which contains daily files with four epochs at a degree spacing of $2.5° \times 2.5°$, based on the method outlined in Van Dam and Wahr (1987) and van Dam (2010). To enable compatibility with the obtained GPS daily solutions, we have averaged the 6-hourly atmospheric loading data set to produce daily solutions. Subsequently, the residual GPS deformation time series was obtained utilizing these two sets of daily solutions (GPS and atmospheric loading solutions).

In the second step, the computed loosely constrained solutions were then passed to GLOBK to estimate station positions, velocities, orbital and Earth rotation parameters using the Kalman filter approach. We have used the standard set of IGS sites for reference frame realization in ITRF2008. It is important to note that while processing the GPS data using the GAMIT/GLOBK, we did not account for hydrological loading effects; hence, the surface deformation induced by this effect still exists in the residual GPS deformation time series, also henceforth referred as GPS signal.

2.2. GRACE Data

The GRACE satellite gravity mission launched in March 2002 is designed to detect changes in mass by sensing perturbations of the Earth's gravity field induced by continental hydrology, melting of ice, etc. and provide the anomalies in terms of equivalent water height (EWH) or in the form of terrestrial water storage (Tapley et al., 2004; Wahr et al., 1998). The EWH deviations monitored by GRACE include the collective contributions of groundwater, soil water, surface water, snow, ice, and biomass. To compute the effect of hydrological seasonal loading changes and to remove it from the GPS signal (time series), we have used the monthly solutions of the GRACE spherical harmonic field product RL03 provided by the French agency Groupe de Recherche en Géodésie Spatiale (GRGS) (Lemoine et al., 2013). In the monthly products, the

Degree-1 coefficients of geocenter motion were replaced by the Stokes coefficients derived by Swenson et al. (2008). To reduce the contribution of noise in higher degree coefficients, the GRACE data were postprocessed using destriping and Gaussian smoothing filters as suggested by Swenson and Wahr (2006). To generate the anomaly coefficients, we used coefficient of the spherical harmonic models and converted the spherical harmonic models into mass change in terms of EWH. The spherical harmonic coefficients are in degree and order 80, corresponding to a (half-wavelength) spatial resolution of approximately 250 km (Wahr et al., 1998).

The vertical and horizontal surface deformations or displacements due to mass variations were obtained from the inversion of spherical harmonic coefficients of gravity signals (Wahr et al., 1998). Farrell (1972) expressed the horizontal elastic deformation as follows:

$$H(\theta,\lambda,t) = R\sum_{l=1}^{\infty}\sum_{m=0}^{l} P_{lm}(cos\ \theta).[\Delta C_{lm}(t)\cos m\lambda + \Delta S_{lm}(t)\sin m\lambda].\frac{l_l}{1+k_l} \quad (1)$$

Davis et al. (2004) expressed the vertical elastic deformations as follows:

$$V(\theta,\lambda,t) = R\sum_{l=1}^{\infty}\sum_{m=0}^{l} P_{lm}(cos\ \theta).[\Delta C_{lm}(t)\cos m\lambda + \Delta S_{lm}(t)\sin m\lambda].\frac{h_l}{1+k_l} \quad (2)$$

where θ and λ are the colatitude and longitude of the point observed at time *t, R* is the Earth radius, *l* and *m* are the degree and order of the spherical harmonic model, P_{lm} is fully normalized Legendre functions, $\Delta C_{lm}(t)$ and $\Delta S_{lm}(t)$ are the spherical harmonic coefficient anomalies from GRACE, and h_l and k_l are elastic load Love numbers (Pagiatakis, 1990). The hydrologically induced seasonal variations at each GPS location were estimated with respect to the center of mass of the Earth as described in equation (2) (Fu & Freymueller, 2012). To destripe the correlated GRACE error and leakage bias from GRACE mass change (Chen et al., 2015), we employed the Gaussian smoothing with a radius of 250-km window and global forward modeling on a regional average basis, respectively.

Figure 2 represents the spatial secular variation trend of mass change (EWH) estimated from the spherical harmonic coefficients of GRACE data over the study area corresponding to January 2004 to January 2015 (excluding a total 5 months; that is, January 2011, October 2012, and March, August, and September 2013, where data were not available). The EWH map in Figure 2 shows the spatial secular variation trend of EWH with two significant negative secular trends in the NW and NE sectors of India (blue areas in Figure 2). The GRACE-derived hydrological induced displacements in vertical and horizontal directions are indicated as circles and vectors, respectively.

2.3. Common Mode Errors

Common mode errors exist in GPS time series and are one of the major sources affecting the accuracy and reliability of the position coordinates and secular trend of any GPS location (Nikolaidis, 2002; Wdowinski et al., 1997). Among the discussed contributing components to the GPS signal in the introductory section, the seasonal variations and antenna offsets are the prominent common mode errors. The seasonal signals are modeled by the first and second harmonics of a sine function, and the model is then subtracted from the observed time series.

The secular trend, which represents the strain accumulation due to interseismic plate motion, is obtained utilizing the following analytical function proposed by Nikolaidis (2002), Herring (2003), and Tian (2011):

$$d(t) = c + \nu t + X\sin(\omega t + \varphi_1) + Y\sin(2\omega t + \varphi_2) + a\left[\ln\left(1 + t/\tau_{\log}\right)\ \text{or/and}\ \left(1 - e^{-(t/\tau\exp)}\right)\right] \quad (3)$$

where *d(t)* is the displacement as a function of time *t*, ν the linear velocity, *c* the coseismic offset, *X* the amplitude of the annual cycle, φ_1 the phase offset of the annual cycle, *Y* the amplitude of the semiannual cycle, φ_2 the phase offset of the semiannual cycle, $\omega = 2\pi/T$, *a* the amplitude of postseismic decay, $\tau_{\log}$ the decay time corresponding to logarithmic decay, and $\tau_{\exp}$ is the decay time corresponding to exponential decay. The resulting vertical and horizontal secular motions of all GPS sites in ITRF2008 were estimated using the least squares method (Tian, 2011) and are shown in Figures 3 and supporting information Figure S1. The uncertainties of the parameter estimates are calculated using the sigmas of the coordinate estimates in the time series with either white or flicker noise assumptions (Herring, 2003).

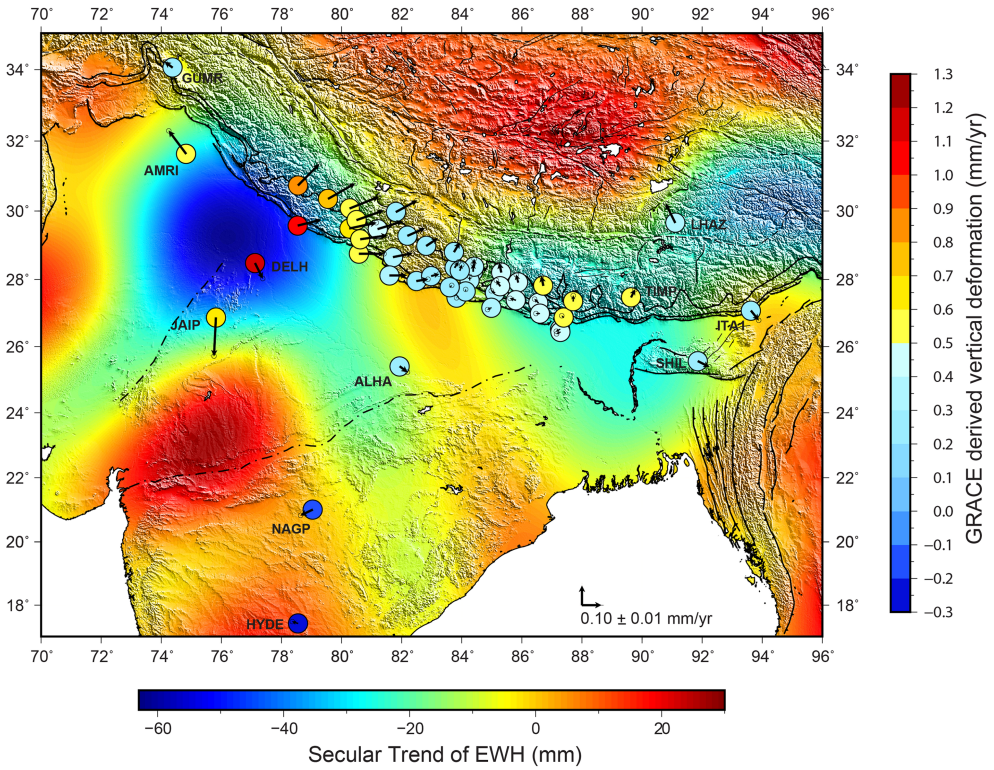

Figure 2. The background color shaded relief map illustrates the secular trend of GRACE-derived hydrological mass variations in terms of equivalent water height (EWH) in mm (horizontal color bar) of the study area spanning from 2004 to 2015. The circles represent the GRACE-derived vertical deformation in millimeters per year (vertical color bar). The arrows indicate the GRACE-derived horizontal deformation in millimeters per year.

In order to obtain the improved time series that contains tectonic motion with linear/secular components, all common mode seasonal variations were accounted using equation (3). Thus, corrected GPS position time series in vertical, east-west, and north-south components are compared with the GRACE-derived elastic deformation time series (Figure 3). The surface mass deformations obtained from GRACE in E-W, N-S, and vertical are used for separating the tectonic deformation from the respective GPS velocity components.

3. Results and Discussion

3.1. Qualitative analysis of Seasonal Signals

Preliminary evaluation of GPS and GRACE time series of vertical, E-W, and N-S components shows that seasonal variations of vertical displacements are most significant in both time series (Figures 3, and S1). In order to visualize and compare the time series and models of GPS and GRACE data, we present the vertical components of detrended GPS and GRACE time series with 1σ standard deviations from selected GPS sites for the different terrain conditions at Sites HYDE, ALHA, SHIL, and DELH located at Hyderabad (south India), Allahabad (IGP, North India), Shillong (NE India), and Delhi (North India), respectively and at sites GHUT, CHLM, TIMP, and LHAZ located in the Kumaon Himalaya, Nepal Himalaya, Sikkim Himalaya, and Tibetan Plateau, respectively (Figures 3). The correlation coefficients obtained for vertical, E-W and N-S components of GPS and GRACE signals give average values of 0.86, 0.59, and 0.71, respectively (Table 1). While comparing the vertical and horizontal seasonal signals together, the horizontal components give an average value of 0.64 against the vertical value of 0.86. Hence, the further quantitative analysis and discussions are focused mostly in terms of vertical displacements.

Considering the spatially varying geological terrain conditions in the study area, it may be noted that in the entire central Himalayan region (sites north of MFT, i.e., BESI, DLPA, DNSG, DRCL, GRHI, KIRT, PYUT, RMJT, RMTE, SMKT, SNDL, SRNK, BYNA, CHLM, DMAU, GHER, GUMB, JMLA, KKN4, KLDN, SYBC, TIMP, JMSM, ODRE, TPLJ, GNTW, GHUT, WIH2, BDRI, MUNS, BMC, TIMP, and LHAZ), the GPS- and

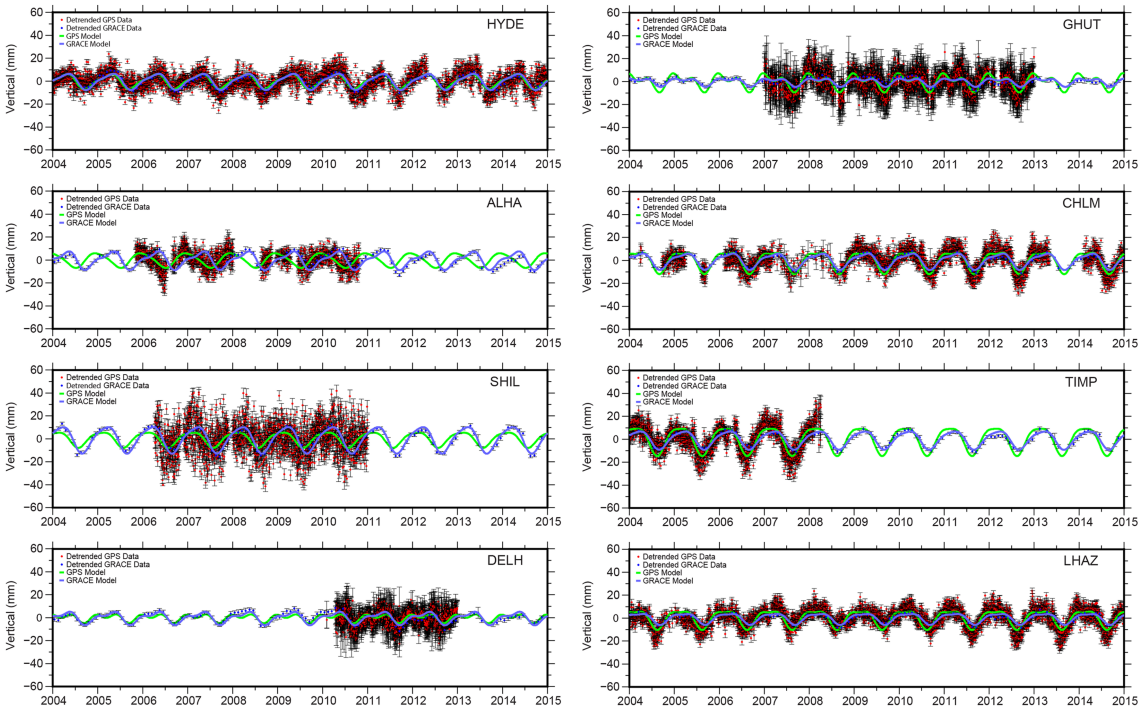

Figure 3. (left column) Comparison of detrended GPS- and GRACE-derived seasonal vertical displacements from different terrain conditions at sites HYDE, ALHA, SHIL, and DELH located at Hyderabad (south India), Allahabad (IGP, North India), Shillong (NE India), and Delhi (North India), respectively (Figure 1). Red dots with error bars represent the detrended GPS data, and blue dots with error bars represent the monthly averaged detrended GRACE data. Green and blue lines indicate the best fit models (annual and semiannual components) for GPS and GRACE data. (right column) Comparison of detrended GPS- and GRACE-derived seasonal vertical displacements from different terrain conditions at sites GHUT, CHLM, TIMP, and LHAZ located in the Kumaon Himalaya, Nepal Himalaya, Sikkim Himalaya, and Tibetan Plateau, respectively (Figure 1). Red dots with error bars represent the detrended GPS data, and blue dots with error bars represent the monthly averaged detrended GRACE data. Green and blue lines indicate the best fit models (annual and semiannual components) for GPS and GRACE data.

GRACE-derived displacement time series show a very good correlation with a value of 0.91 with respect to seasonal signals in the vertical component. However, they have a less correlation in horizontal components with a value of 0.69, whereas westernmost and easternmost Himalayan Sites GUMR and ITA1 show a less correlation values of 0.68 and 0.63 in vertical components and 0.24 and 0.31 in horizontal components, respectively. While considering the sites over IGP (south of MFT, i.e., BHTW, DNGD, NPGJ, BELT, SIM9, BRN2, BRNG, and ALHA), the correlation for vertical and horizontal components is found to be 0.85 and 0.58, respectively. However, in the North Indian sector surrounding IGP, the Sites AMRI, JAIP, and DELH located at the northwestern part of the study area show the average correlation values of 0.78 and 0.57 for vertical and horizontal components, respectively. The northeastern Indian Site SHIL shows the correlation values of 0.82 in vertical and 0.44 in horizontal components. The Sites NAGP and HYDE located south of IGP show the average correlation values of 0.97 and 0.58 for vertical and horizontal components, respectively.

3.2. Quantitative Analysis of Amplitude and Phase Variations

The Himalaya and IGP receive large amounts of water from precipitation (monsoon), rivers, and glaciers. Hydrological mass loads are believed to manifest as strong seasonal signals over the Nepal Himalaya and surroundings (Bettinelli et al., 2008; Fu & Freymueller, 2012; Pan et al., 2018). Due to these effects, the subsurface water mass loads tend to fluctuate periodically throughout the year. Hence, the amplitude and phase of this seasonal signal in GPS and GRACE observations (Figures 3a, 3b, and S1) can be computed in terms of hydrological mass variations.

First, to compare the annual amplitudes between GPS- and GRACE-derived seasonal signals, we fit both vertical displacement from GPS and GRACE using the weighted least squares method (Krystek & Anton, 2007).

Table 1
Tectonic Zones, GPS Station Names, Latitude, Longitude, and Correlation Coefficient Values Obtained Between GPS and GRACE Signal for North, East, and Vertical Components

				Correlation coefficient		
Tectonic zones	Station	Latitude	Longitude	North	East	Vertical
Western Himalaya	GUMR	34.056	74.375	0.194	0.2783	0.6772
North India	AMRI	31.635	74.825	0.3505	0.6163	0.6854
	DELH	28.48	77.12	0.9128	0.1703	0.8834
	JAIP	26.87	75.818	0.6954	0.7046	0.7843
Indo-Gangetic Plain	DNGD	28.754	80.582	0.6649	0.0509	0.5827
	NPGJ	28.117	81.595	0.9217	0.7569	0.9803
	BELT	27.457	83.826	0.1325	0.0797	0.8372
	SIM9	27.165	84.984	0.5475	0.902	0.8667
	BRN2	26.52	87.272	0.5261	0.8271	0.9623
	BRNG	26.439	87.281	0.7189	0.9337	0.2853
	BHTW	29.577	78.545	0.8075	0.4514	0.7039
	ALHA	25.408	81.936	0.0391	0.9258	0.7588
Central Himalaya	BDRI	29.492	80.26	0.9118	0.9212	0.5032
	GHUT	30.736	78.55	0.9615	0.9556	0.9286
	MUNS	30.349	79.553	0.6735	0.2157	0.7171
	WIH2	30.072	80.27	0.85	0.7409	0.9409
	LHAZ	29.657	91.104	0.8801	0.0821	0.8884
	BESI	28.229	84.38	0.8141	0.5617	0.9983
	BMCL	28.656	81.714	0.7169	0.5503	0.9629
	BYNA	29.474	81.201	0.988	0.4619	0.9865
	CHLM	28.207	85.314	0.9521	0.5772	0.977
	DAMA	27.608	85.108	0.8089	0.8617	0.9671
	DLPA	28.984	82.818	0.5385	0.3388	0.9478
	DMAU	27.973	84.265	0.8648	0.1285	0.9986
	DNSG	28.345	83.763	0.8926	0.7151	0.938
	DRCL	29.734	80.501	0.9498	0.7777	0.7557
	GHER	28.375	84.41	0.9752	0.8571	0.6886
	GNTW	29.177	80.626	0.9156	0.9268	0.9043
	GRHI	27.951	82.491	0.8424	0.2134	0.9599
	GUMB	27.91	85.877	0.9343	0.4019	0.9819
	JMLA	29.278	82.193	0.7531	0.15	0.921
	JMSM	28.805	83.743	0.9328	0.8252	0.9816
	KAWA	27.648	84.13	0.9377	0.6588	0.5606
	KKN4	27.801	85.279	0.639	0.3164	0.9534
	KLDN	27.767	83.603	0.7332	0.8889	0.9822
	ODRE	26.866	87.392	0.813	0.6862	0.9921
	PYUT	28.101	82.987	0.5805	0.7016	0.9498
	RMJT	27.305	86.55	0.644	0.1696	0.9667
	RMTE	26.991	86.597	0.514	0.3317	0.9791
	SMKT	29.969	81.807	0.7377	0.8622	0.8999
	SNDL	27.385	85.799	0.7198	0.4727	0.9921
	SRNK	28.26	83.936	0.6786	0.8292	0.8772
	SYBC	27.814	86.712	0.8493	0.8111	0.9911
	TIMP	27.472	89.635	0.8968	0.7529	0.9315
	TPLJ	27.352	87.71	0.8844	0.3957	0.9981
North East India	SHIL	25.563	91.855	0.2344	0.6552	0.8174
	ITA1	27.075	93.626	0.5223	0.0882	0.6254
South India	NAGP	21.010	79.040	0.3756	0.9126	0.9753
	HYDE	17.417	78.551	0.107	0.9576	0.9705
	IISC	13.021	77.570	0.4233	0.7032	0.9178

It is estimated that the entire region (i.e., Himalaya and North Indian sectors together) yields a slope value of 0.76 (Figure 4). However, to compare our result with that of Fu and Freymueller (2012) (slope value 0.9), from Nepal Himalaya, we separately estimated the slope value pertaining to Nepal and NW Himalayas together, which yield a value of 0.85 (Figure 4). It is pertinent to note that the Himalayan sector

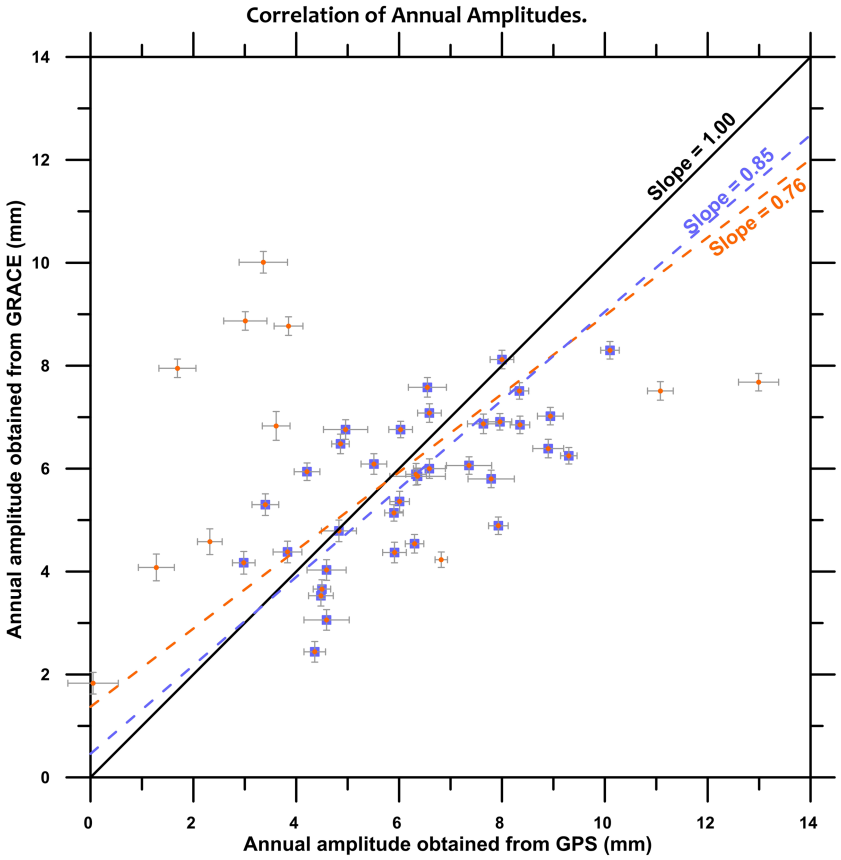

Figure 4. Correlation between annual amplitude estimated from the seasonal signals observed in GPS and GRACE measurements. The black continuous line shows the ideal condition in which GPS and GRACE perfectly match each other (slope = 1). The orange dash line indicates the estimated best fit line to the GPS and GRACE data for the entire GPS network (orange color data points). The blue dash line indicates the estimated best fit line to the GPS and GRACE data for GPS sites in Nepal and NW Himalaya for the comparison of result with Fu and Freymueller (2012) (orange data points with blue square).

encompasses almost similar terrain and climatic conditions, whereas the North Indian sector does not. However, the overall slope value of 0.76 indicates the prominence of hydrological mass variations in the study region.

To understand the role of hydrological dominance spatially, further, we compared the amplitude and phase delay of both signals at each site which are represented in color-coded rotating phasor diagrams (Figure 5). Red color indicates the area of GRACE signal dominance, and blue color indicates the dominant area of GPS signal. The extent of shaded portion of the rotating phasor depicts the phase delay in degrees between the GPS and GRACE vertical signals. The larger the phase delay, the smaller the correlation between these two signals and consequently lesser the effect of hydrological mass variations. It may be noted in Figure 5 that the majority of the sites show the phase difference within the limits of conventional phase lag (±25° to ±30°) (van Dam et al., 2007).

The sites over the IGP and sub-Himalaya are well influenced by the associated seasonal hydrological loading effects (red phasors in Figure 5), whereas the neighboring sites of IGP represent the low influence of hydrological effects (blue phasors). However, the sites JAIP and AMRI in red phasors, characterized with larger phase lags of 59° and 89° (Figures 5) along with low correlation coefficients of 0.78 and 0.68 (Table 1), respectively, show the less reliability of hydrological influence between GPS and GRACE signals over the locations. The Site GUMR located at the western Himalaya shows the maximum phase lag of 127° (Figure 5), which could be due to the GPS site instability associated to snow accumulation, as evident from the scattering of GPS position time series of GUMR (Figure S1).

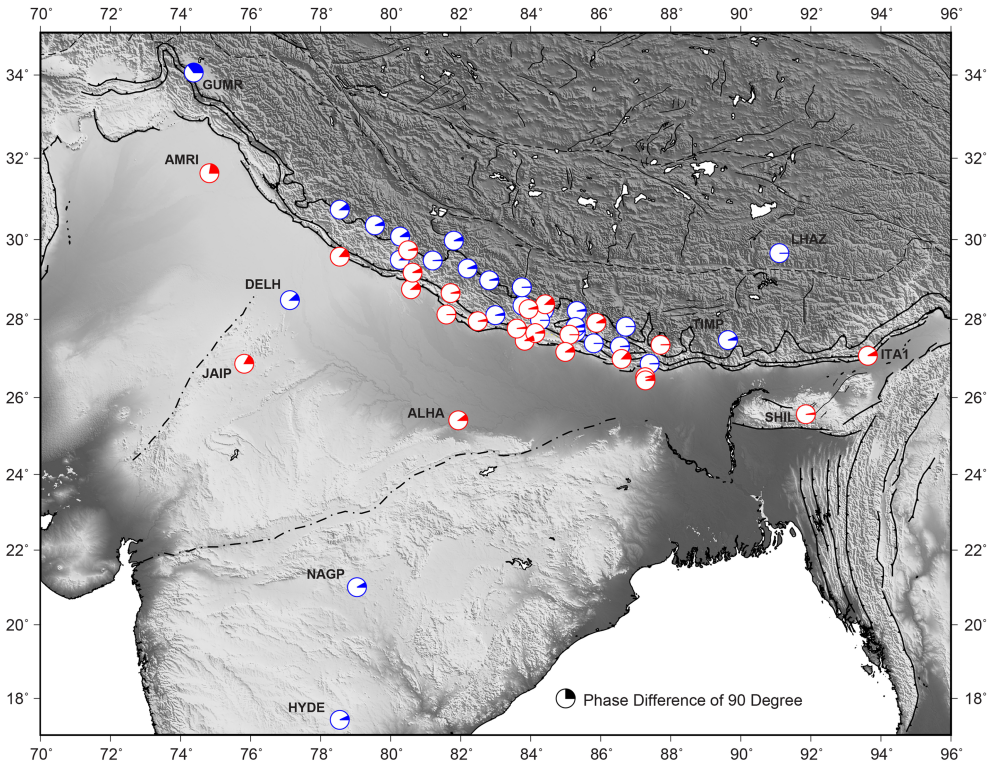

Figure 5. The figure illustrates the relative dominance in seasonal annual amplitude for GPS and GRACE signals along with estimated phase difference between the two geodetic signals represented in colored rotating phasor diagram. Blue colored rotating phasor indicates dominance of seasonal annual amplitude in GPS signal and red colored rotating phasor indicates dominance of seasonal annual amplitude in GRACE signal. The shaded region represents the phase difference between GPS and GRACE signals measured counter clockwise from east direction.

3.3. Consistency in Seasonal Variations

To appraise the consistency in common mode seasonal variations in both GPS and GRACE measurements, a quantitative check was carried out by computing the reduction ratio of weighted root-mean-square (WRMS) based on equation (4) (Fu et al., 2012; Tesmer et al., 2011; Tregoning et al., 2009; van Dam et al., 2007). The WRMS reduction is commonly used to quantify the influence of elastic deformation (GRACE signals) over the tectonic deformation (GPS signals) (van Dam et al., 2007).

$$WRMS_{reduction} = \frac{WRMS_{GPS} - WRMS_{GPS-GRACE}}{WRMS_{GPS}} \quad (4)$$

$WRMS_{GPS}$ is the WRMS value measured for the GPS time series, while $WRMS_{GPS\text{-}GRACE}$ is that measured for GRACE seasonal model-reduced GPS time series.

Figure 6 shows the WRMS percentage reductions estimated for the vertical component. Please refer to Figure S2 for the WRMS reduction plots for both E-W and N-S components. Table 2 shows the list of GPS stations and their corresponding WRMS reduction ratio, which is expressed as a percentage of all three components. Since seasonal signals are prevalent in the vertical component (Figure 3), significant reduction in WRMS is noticed for the same component. We find that the reduction is not significant for the E-W and N-S components (Figures S2). It may be noted that the presence of seasonal signals with large variation in amplitude shall enlarge the WRMS value (Tregoning & van Dam, 2005). Large values in WRMS reduction at sites or components indicate that a good agreement between GPS and GRACE displacements exists in terms of hydrological mass influence at these locations. On the other hand, negative values indicate disagreement between the tectonic and elastic deformation, which are mostly observed in the horizontal components. The average WRMS reduction values for vertical, E-W and N-S components for the study region are

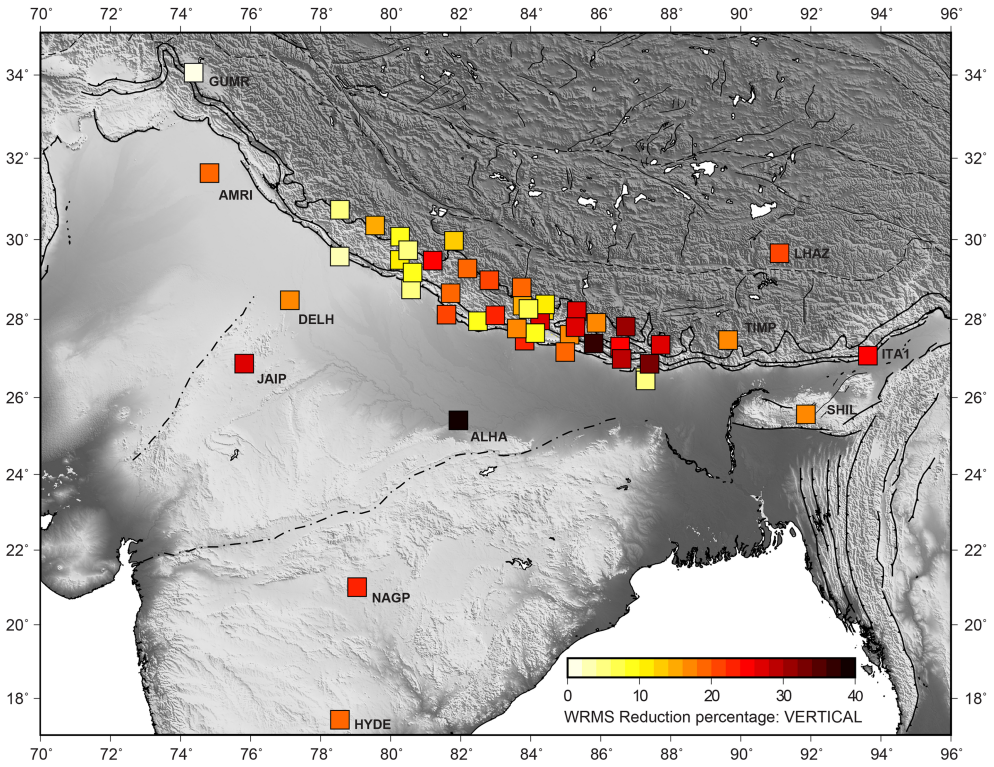

Figure 6. WRMS reduction in percentage estimated for detrended GPS vertical deformation after removing GRACE-derived detrended vertical deformation at all GPS locations (square) in the study area.

17.72%, −1.08%, and −7.13%, respectively. The vertical components show substantial reduction compared to the east and north components (Figures 6, S2a, and S2b). Interestingly, most of the sites located over the IGP exhibit large positive WRMS reduction values in the vertical component (a minimum of 3.96% and a maximum value of 40% for IGP, constituting an average value of 15.16%). This suggests that IGP has significant hydrological mass variation effects (Figure 6). However, the sites located at Kumaun and Garhwal Himalaya (west of Nepal Himalaya) altogether show a less reduced percentage. This could be due the predominant interannual variations observed at these sites compared to a majority of Nepal Himalayan sites (Figure S1). The smallest reduction rate observed at GUMR (0.79%) in western Himalaya could be due to the local effects such as 50% reduction of the annual rainfall from Indian monsoon and seasonal snow accumulation or discharge in the area (Bookhagen & Burbank, 2010; Hao et al., 2016). However, the moderate reduction rates (~20% to ~30%) between GPS and GRACE surrounding the IGP is attributed to a stable geologic terrain condition, where the deformation due to seasonal hydrological variations is relatively low.

3.4. Hydrologic-Corrected Deformation and Slip Rate Modeling

The seasonal hydrological loading and unloading over the continents deform the Earth surface elastically (Farrell, 1972). As reported in the Himalaya and elsewhere, these seasonal signal contributions from hydrological mass variations affect the position time series and velocities of GPS stations (i.e., up to 2 mm for horizontal and 4 mm for vertical) (Blewitt & Lavallée, 2002). In order to estimate the tectonic-related linear motion, we removed the GRACE-derived vertical and horizontal deformation rates from the GPS-derived counterparts (Table 3). Figures 7 and S3 illustrate the vertical and horizontal linear secular rates of the Indian plate velocity in terms of hydrologically corrected GPS velocity vectors. The GRACE-corrected vertical deformation illustrated in Figure 7 reveals two distinct deformation patterns. The sites located over the sub-Himalaya and IGP show a subsidence trend. The sites neighboring IGP and higher Himalaya (i.e., north of MBT, south of IGP, and NW and NE Indian sectors) depict an uplift trend (Figure 8). Considering the GPS data from the Nepal Himalaya, Fu and Freymueller (2012) and Pan et al. (2018) showed a similar pattern and

Table 2
Tectonic Zones, GPS Station Names, Latitude, Longitude, Epoch Duration, and WRMS Reduction Percentage for North, East, and Vertical Components

					WRMS reduction percentage		
Tectonic zones	Station	Latitude	Longitude	Epoch duration	North	East	Vertical
Western Himalaya	GUMR	34.056	74.375	2005.823–2010.201	−0.40	0.24	0.79
North India	AMRI	31.635	74.825	2005.804–2009.943	−11.71	1.64	19.59
	DELH	28.48	77.12	2010.091–2012.998	−22.92	−6.67	16.16
	JAIP	26.87	75.818	2005.815–2010.417	−22.22	6.42	26.48
Indo-Gangetic Plain	DNGD	28.754	80.582	2008.345–2014.997	−15.00	−0.44	4.00
	NPGJ	28.117	81.595	2007.381–2014.997	8.97	1.62	21.90
	BELT	27.457	83.826	2002.512–2012.971	−5.53	−3.51	22.40
	SIM9	27.165	84.984	2002.001–2005.371	−16.46	4.61	18.11
	BRN2	26.52	87.272	2009.385–2014.997	−11.76	4.82	5.09
	BRNG	26.439	87.281	2004.199–2009.377	−12.61	2.05	5.79
	BHTW	29.577	78.545	2006.001–2012.998	−9.04	−0.59	3.96
	ALHA	25.408	81.936	2005.845–2010.811	−24.78	4.67	40.00
Central Himalaya	BDRI	29.492	80.26	2007.521–2012.998	−23.79	−5.71	10.17
	GHUT	30.736	78.55	2007.001–2012.998	6.55	−9.16	5.43
	MUNS	30.349	79.553	2006.001–2009.689	2.63	−0.52	15.78
	WIH2	30.072	80.27	2006.001–2012.998	−7.22	−7.88	9.99
	LHAZ	29.657	91.104	2002.001–2014.997	−4.91	−6.52	17.15
	BESI	28.229	84.38	2008.490–2013.185	−40.14	−8.94	12.49
	BMCL	28.656	81.714	2007.208–2014.997	−6.93	5.54	19.95
	BYNA	29.474	81.201	2009.292–2012.490	14.89	−4.07	24.44
	CHLM	28.207	85.314	2004.249–2014.997	7.22	2.20	26.64
	DAMA	27.608	85.108	2002.001–2011.737	0.00	1.97	16.65
	DLPA	28.984	82.818	2007.356–2013.245	−8.47	−2.67	21.94
	DMAU	27.973	84.265	2008.509–2012.826	0.00	−6.03	27.61
	DNSG	28.345	83.763	2012.325–2014.997	1.08	5.15	15.89
	DRCL	29.734	80.501	2008.197–2014.997	8.66	−5.40	4.35
	GHER	28.375	84.41	2008.503–2013.029	9.73	−7.52	10.30
	GNTW	29.177	80.626	2008.328–2014.997	0.36	7.88	8.28
	GRHI	27.951	82.491	2007.345–2014.997	−20.54	−2.50	9.48
	GUMB	27.91	85.877	2002.001–2011.739	11.43	−8.29	17.53
	JMLA	29.278	82.193	2007.370–2014.997	−4.37	−0.94	18.13
	JMSM	28.805	83.743	2004.339–2014.997	−2.68	−1.37	19.95
	KAWA	27.648	84.13	2008.509–2011.479	7.81	4.37	9.28
	KKN4	27.801	85.279	2004.221–2014.997	−5.82	−5.02	26.40
	KLDN	27.767	83.603	2004.282–2014.997	−8.05	8.30	17.65
	ODRE	26.866	87.392	2004.856–2013.420	−1.98	−3.60	33.60
	PYUT	28.101	82.987	2011.241–2014.997	−9.23	4.04	22.46
	RMJT	27.305	86.55	2009.845–2013.593	−2.04	−4.18	24.78
	RMTE	26.991	86.597	2008.977–2014.997	−7.08	−1.00	28.16
	SMKT	29.969	81.807	2008.372–2014.997	−16.04	7.89	13.69
	SNDL	27.385	85.799	2011.258–2014.997	−9.06	−0.78	36.16
	SRNK	28.26	83.936	2005.286–2012.427	−2.64	−10.29	7.08
	SYBC	27.814	86.712	2008.758–2014.997	−1.92	2.05	30.26
	TIMP	27.472	89.635	2002.384–2008.257	0.98	−0.77	17.42
	TPLJ	27.352	87.71	2004.188–2014.997	6.92	−3.49	27.71
North East India	SHIL	25.563	91.855	2006.272–2010.997	−9.43	−1.81	17.34
	ITA1	27.075	93.626	2005.891–2010.149	−3.65	−13.79	24.66
South India	NAGP	21.010	79.040	2005.817–2010.724	−31.77	1.38	22.06
	HYDE	17.417	78.551	2002.825–2014.997	−17.24	0.31	20.50
	IISC	13.021	77.570	2002.006–2014.997	−20.91	−2.02	18.19

interpreted in terms of the Indian plate underthrusting the Eurasian plate during the interseismic period. However, in the present study it is evident that all of the sites located over the IGP south of MFT, including the farthest site (ALHA, located at a distance of ~280 km south of the MFT), also show a similar trend of subsidence. It is interesting to note that the sites located between the MFT and MBT (sub-Himalaya) (i.e., GNTW, BMCL, GRHI, PYUT, BELT, SNDL, RMTE, and ODRE) show an average subsidence rate of 1.14

Table 3
Tectonic Zones, GPS Station Names, Latitude, Longitude, and GRACE-Corrected GPS Velocities in ITRF 2008 for North, East, and Vertical Components

				GRACE-reduced/corrected GPS velocity (mm/year)		
Tectonic zones	Station	Latitude	Longitude	North	East	Vertical
Western Himalaya	GUMR	34.056	74.375	32.16 ± 0.14	27.39 ± 0.19	5.61 ± 0.78
North India	AMRI	31.635	74.825	33.73 ± 0.04	30.87 ± 0.04	3.69 ± 0.20
	DELH	28.48	77.12	33.76 ± 0.06	34.30 ± 0.09	0.36 ± 0.23
	JAIP	26.87	75.818	33.18 ± 0.03	34.62 ± 0.03	5.62 ± 0.13
Indo-Gangetic Plain	DNGD	28.754	80.582	34.82 ± 0.03	37.82 ± 0.03	−3.02 ± 0.09
	NPGJ	28.117	81.595	35.78 ± 0.03	36.58 ± 0.02	−1.58 ± 0.08
	BELT	27.457	83.826	35.37 ± 0.06	36.33 ± 0.05	−0.50 ± 0.19
	SIM9	27.165	84.984	34.80 ± 0.09	37.48 ± 0.08	−1.41 ± 0.30
	BRN2	26.52	87.272	33.03 ± 0.04	39.36 ± 0.04	−3.21 ± 0.13
	BRNG	26.439	87.281	34.25 ± 0.06	39.10 ± 0.07	−2.79 ± 0.28
	BHTW	29.577	78.545	31.84 ± 0.02	47.46 ± 0.04	−0.78 ± 0.09
	ALHA	25.408	81.936	35.40 ± 0.02	39.05 ± 0.03	−1.04 ± 0.11
Central Himalaya	BDRI	29.492	80.26	22.76 ± 0.03	28.32 ± 0.05	1.67 ± 0.11
	GHUT	30.736	78.55	30.40 ± 0.03	31.53 ± 0.04	1.06 ± 0.09
	MUNS	30.349	79.553	29.61 ± 0.07	26.95 ± 0.09	1.63 ± 0.26
	WIH2	30.072	80.27	34.13 ± 0.02	33.21 ± 0.03	0.64 ± 0.09
	LHAZ	29.657	91.104	15.23 ± 0.01	46.52 ± 0.01	1.26 ± 0.05
	BESI	28.229	84.38	30.85 ± 0.06	36.38 ± 0.06	1.68 ± 0.22
	BMCL	28.656	81.714	33.11 ± 0.02	34.78 ± 0.02	−1.45 ± 0.06
	BYNA	29.474	81.201	26.34 ± 0.06	34.82 ± 0.09	1.50 ± 0.19
	CHLM	28.207	85.314	26.61 ± 0.02	37.14 ± 0.02	3.75 ± 0.05
	DAMA	27.608	85.108	34.27 ± 0.02	37.64 ± 0.02	0.42 ± 0.08
	DLPA	28.984	82.818	24.72 ± 0.03	34.27 ± 0.03	3.21 ± 0.08
	DMAU	27.973	84.265	33.96 ± 0.06	37.45 ± 0.06	−0.20 ± 0.21
	DNSG	28.345	83.763	27.87 ± 0.11	36.71 ± 0.10	3.38 ± 0.36
	DRCL	29.734	80.501	29.84 ± 0.04	31.80 ± 0.04	1.46 ± 0.20
	GHER	28.375	84.41	27.80 ± 0.09	36.12 ± 0.10	4.45 ± 0.43
	GNTW	29.177	80.626	33.29 ± 0.03	34.04 ± 0.04	−2.39 ± 0.13
	GRHI	27.951	82.491	33.68 ± 0.03	37.07 ± 0.03	−0.74 ± 0.09
	GUMB	27.91	85.877	27.70 ± 0.02	37.02 ± 0.01	3.93 ± 0.06
	JMLA	29.278	82.193	25.63 ± 0.02	33.33 ± 0.02	1.88 ± 0.07
	JMSM	28.805	83.743	25.18 ± 0.02	35.75 ± 0.02	2.69 ± 0.05
	KAWA	27.648	84.13	34.84 ± 0.08	37.33 ± 0.09	0.85 ± 0.35
	KKN4	27.801	85.279	32.34 ± 0.02	37.05 ± 0.02	0.72 ± 0.05
	KLDN	27.767	83.603	34.33 ± 0.01	37.01 ± 0.01	0.26 ± 0.05
	ODRE	26.866	87.392	35.13 ± 0.02	39.51 ± 0.02	−1.79 ± 0.06
	PYUT	28.101	82.987	32.84 ± 0.06	36.70 ± 0.05	−0.02 ± 0.17
	RMJT	27.305	86.55	30.31 ± 0.08	36.49 ± 0.07	1.32 ± 0.21
	RMTE	26.991	86.597	33.40 ± 0.03	37.11 ± 0.04	−2.07 ± 0.09
	SMKT	29.969	81.807	21.66 ± 0.02	32.59 ± 0.03	2.46 ± 0.07
	SNDL	27.385	85.799	33.40 ± 0.06	36.47 ± 0.06	−0.56 ± 0.16
	SRNK	28.26	83.936	30.63 ± 0.03	36.41 ± 0.03	0.51 ± 0.10
	SYBC	27.814	86.712	24.66 ± 0.02	37.73 ± 0.03	2.20 ± 0.08
	TIMP	27.472	89.635	27.00 ± 0.03	41.96 ± 0.04	−2.39 ± 0.12
	TPLJ	27.352	87.71	29.74 ± 0.02	37.06 ± 0.03	0.91 ± 0.05
North East India	SHIL	25.563	91.855	31.13 ± 0.05	40.88 ± 0.05	3.10 ± 0.23
	ITA1	27.075	93.626	23.43 ± 0.03	42.45 ± 0.03	0.52 ± 0.13
South India	NAGP	21.010	79.040	34.72 ± 0.03	39.30 ± 0.04	1.77 ± 0.14
	HYDE	17.417	78.551	34.79 ± 0.03	40.86 ± 0.03	0.44 ± 0.11
	IISC	13.021	77.570	34.83 ± 0.02	42.08 ± 0.02	0.84 ± 0.07

± 0.12 mm/year. The subsidence rate over the sub-Himalaya could be attributed to the interseismic convergence of the India and Eurasian plates (Fu & Freymueller, 2012; Pan et al., 2018). However, the sites parallel and south of the MFT and over the IGP (BHTW, DNGD, NPGJ, BELT, SIM9, BRN2, and BRNG) show an average subsidence rate double (2.40 ± 0.18 mm/year) that of the sub-Himalaya. Even the farthest GPS site, ALHA at IGP, shows a similar subsidence rate as the sub-Himalaya (1.04 ± 0.11 mm/year), despite

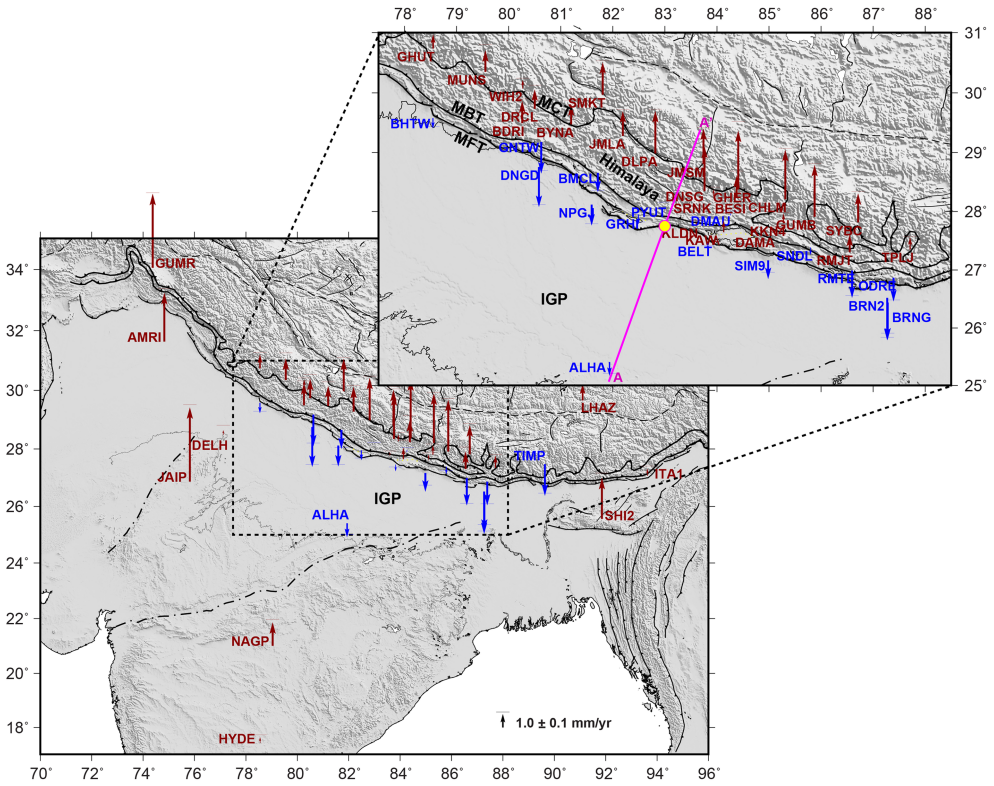

Figure 7. GRACE-corrected secular trend of vertical (vectors) velocities of GPS sites in ITRF2008. The brown and blue arrows indicate uplift and subsidence, respectively. The inset figure represents the zoomed portion of the IGP and Central Himalaya where the locations of the GPS vertical velocities have been used for the 2-D modeling in Figure 9. The magenta color profile line (A-A′) represents the fault-perpendicular profile considered for projection of vertical velocities in Figure 9. The yellow circle indicates the starting location of the MHT, where it is dipping toward the north.

being in a setting where the tectonic influence is likely to be trivial compared to sub-Himalaya. The prominent subsidence rates observed in the IGP region indicate an additional transient component rather than the tectonic or seasonal hydrological deformations as estimated and corrected using GRACE observations. It may be noted that IGP and its surroundings account for the most intensive groundwater-based irrigation in the world (Rodell et al., 2009; Tiwari et al., 2009). Increasing population and associated unsustainable groundwater consumption for irrigation and other anthropogenic uses may attribute to subsidence in the alluvial deposits like IGP (Steckler et al, 2010). To visualize this GRACE-derived hydrological mass variations in terms of EWH- and GRACE-reduced GPS vertical deformation (i.e., tectonic plus transient) over Indian plate, we illustrate the satellite perspective view of the entire area in Figure 8 for better reading.

In order to compute the subsurface slip rate in response to the tectonic forcing, we projected both the GRACE-corrected and uncorrected GPS vertical velocities to NNE-SSW oriented profile (A-A′) perpendicular to the MFT at an azimuth angle of N20°E (inset of Figure 7). For the modeling, we consider 39 stations with uncertainty in vertical velocity less than 0.43 mm/year and which are located within the central Himalaya and IGP within 500 km on either side of Profile A-A′. We observed that the GRACE correction causes reduction in vertical velocity ranging from 0.24 to 1.02 mm/year, resulting in an average reduction rate of 0.42 mm/year (Figure 9). We fit a simple two-dimensional elastic dislocation model (Singh & Rani, 1993) to the vertical GPS profile. A grid search, minimizing the chi-square between the observed and model velocities was used to compute the slip rate and fault locking width for a dip angle of 10°. The model result suggests that most of the vertical GPS velocities could be explained by the interseismic strain from the MHT (Figure 9). Discrepancies in the observed vertical velocities (subsidence trend) along the profile in the lesser Himalayan region are due to large spatial coverage of GPS locations, the projection of the entire vertical velocity to a profile, and lateral variations in strain along the MHT.

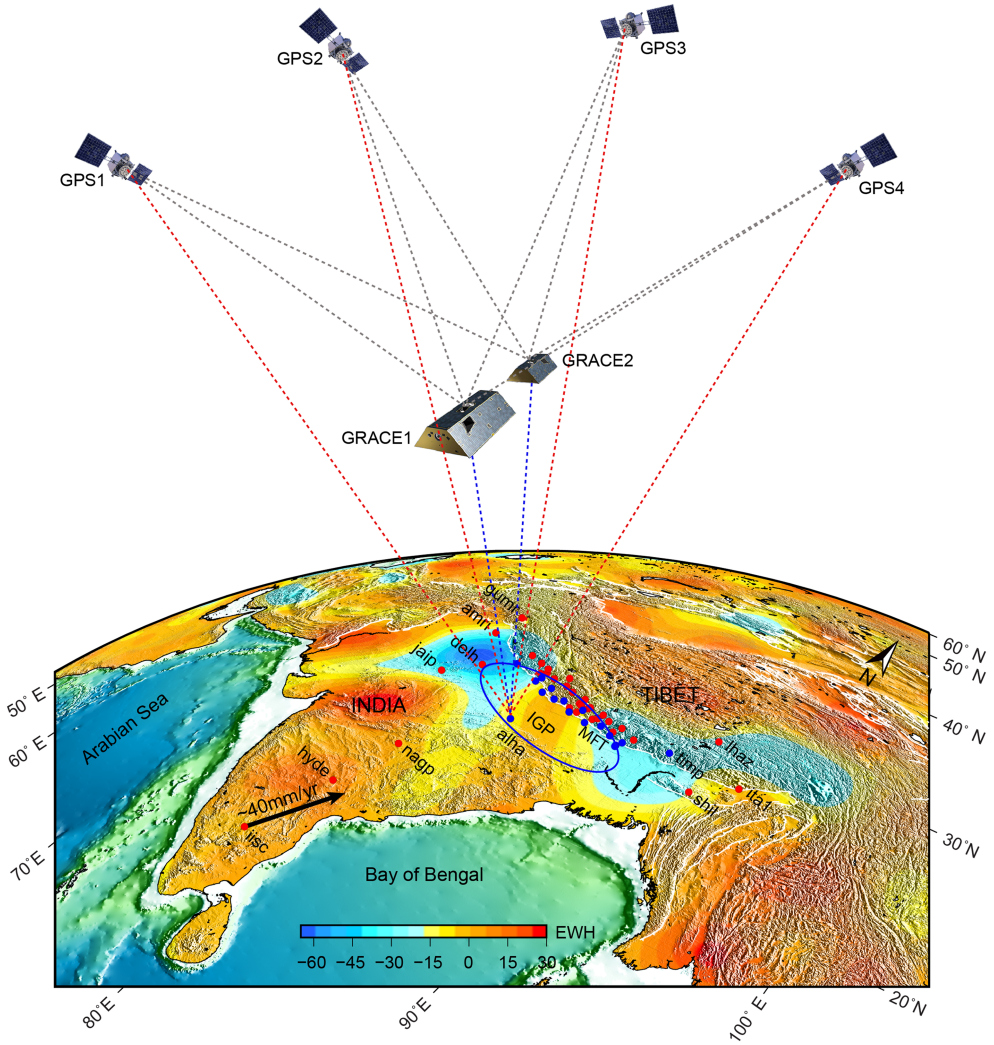

Figure 8. Schematic illustration of the study area in a GPS and GRACE satellite perspective view. The background color shaded relief map illustrates the secular trend of GRACE-derived hydrological mass variations in terms of equivalent water height (EWH) of the study area spanning from 2004 to 2015. Red and blue disks represent the GRACE-corrected GPS uplift and subsidence, respectively. Blue ellipse indicates the zone of subsidence. Black velocity vector indicates the Indian plate motion in Eurasian reference frame at IGS GPS location at IISC, Bangalore, estimated from the velocity in ITRF 2008 (Table 3).

Slip rate estimated from the corrected and uncorrected vertical GPS velocity are 12.4 ± 2.01 and 14.1 ± 1.92 mm/year, respectively, suggesting 12.06% difference in slip rate (i.e., 1.7 mm/year). However, the estimated fault width did not show such significant variations (109.0 ± 4.7 and 108.0 ± 4.6 km for corrected and uncorrected profiles, respectively). We further note that the GRACE corrections to the vertical GPS velocities improve the chi-square misfit by 20.32% (Figures S4). This substantiates the role of hydrological corrections in the estimation of subsurface slip rate. Indeed, hydrological loading and unloading effects due to both seasonal and anthropogenic activities is believed to have a major role in controlling the seasonal stress changes, which modulate the seismicity in the Himalayan collision system (Kundu et al., 2015).

3.5. Other Possible Contributors for Deformation in Himalaya and North India

Besides the significant seasonal variations discussed above, the possible long-term uplift that can contribute toward GRACE- and GPS-derived vertical displacements in the Himalayan region include glacial isostatic adjustments (GIA) and rapid variations in polar motions, respectively (King & Watson, 2014; Matsuo & Heki, 2010). The GIA effect is primarily due to the mass loss in the Himalaya and rapid polar motion is

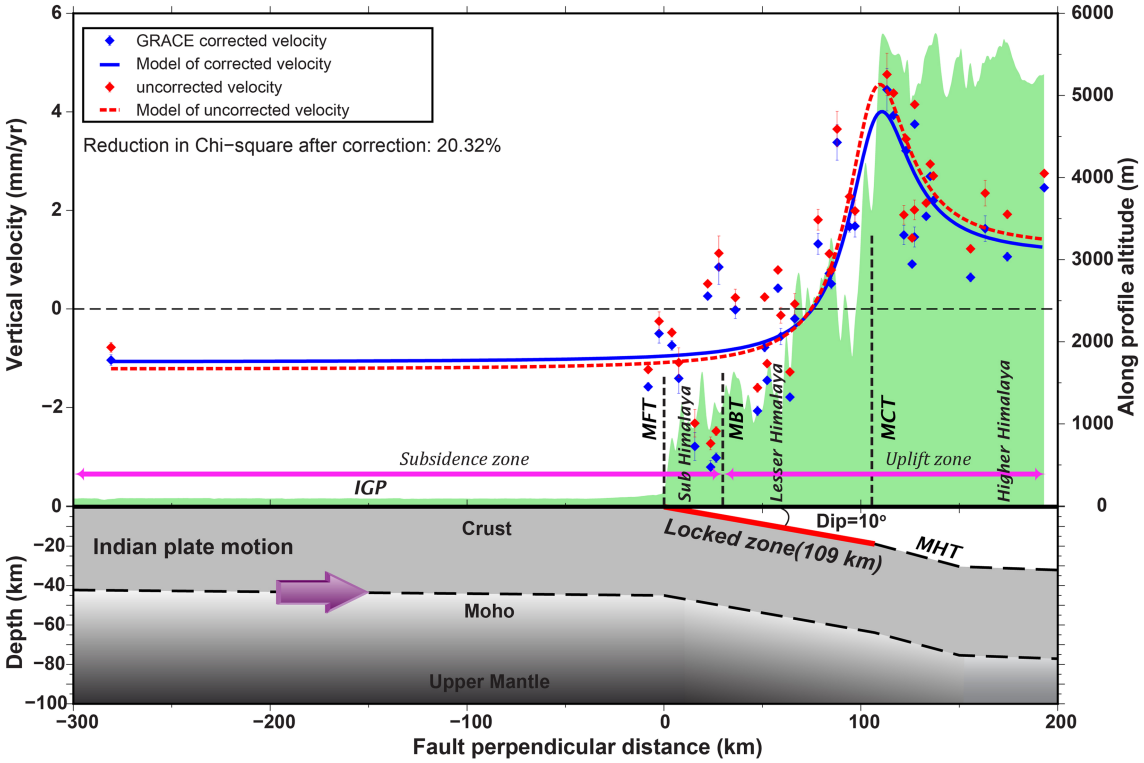

Figure 9. Cross-sectional view of the observed and modelled GPS vertical rates before (red) and after (blue) GRACE correction (please refer to Figure 7 for profile location). The bottom panel depicts the schematic representation of the underthrusting of Indian plate across MHT with assumed dip angle of 10° and estimated locking width of 109 km from MFT.

due to the secular motion of Earth's rotation pole. In this study, we assumed that the GRACE data predominantly reflect nontectonic signals. After detailed analysis of GRACE along with ~900 GPS data, Pan et al. (2018) suggested that the tectonic signals arising from polar motion is negligibly small in the Himalaya and Tibetan Plateau. Hence, we did not attempt to correct for GIA and polar motion effects considering the limited data availability, uncertainties in magnitude, and insignificant secular motion variation, respectively.

4. Conclusions

1. The advantages of using cGPS and GRACE data in tandem are twofold. It enables segregation of contributions from tectonic and nontectonic forces to the crustal deformation. In addition, it provides insights into how the crust deforms due to the interseismic strain accumulation and the influence of seasonal surface mass variations dominated by hydrologic processes.
2. The moderate- to high-level amplitude correlation (slope value of 0.76) and phase delay (degree between ±25° to ±30°) in the vertical component of GPS and GRACE together with average WRMS reduction (17.72%) suggest that the seasonal hydrological mass variation is conspicuous, especially in the sub-Himalaya and IGP.
3. The GPS-derived vertical interseismic deformation corrected for hydrologic mass variations using GRACE observations suggest that the sub-Himalaya and IGP are undergoing subsidence and the surrounding areas show uplift.
4. In addition to the tectonic and nontectonic forcings, unsustainable consumption of groundwater associated to irrigation and other anthropogenic uses influence the subsidence rate in the IGP and sub-Himalaya.
5. The 2-D elastic dislocation modeling using GRACE-corrected and uncorrected GPS vertical velocity suggests that GRACE correction in vertical GPS velocity causes a reduction in the subsurface slip rate estimation over the MHT system by 12.06% and improves the chi-square misfit by 20.32%.

Acknowledgments

The authors thank the Directors of Indian Institute of Geomagnetism (IIG), Space Application Centre (SAC), and Wadia Institute of Himalayan Geology (WIHG) for their permission to carry out this collaborative research. A. P. S. thanks Department of Science and Technology for providing the research fellowship. S. P. S. is supported by CLAIM and NavIC GAGAN UP projects of IIG-DST and SAC-ISRO, respectively. K. M. S. is supported by DMSP R&D and GAP projects of SAC-ISRO. We express our sincere gratitude to Paul Tregoning and Stéphane Bourgogne for the quick response as well as suggestions. We thank Priyesh Kunnummal and Arjun V.H. for extending their help during the formulation of this paper. Raj Kumar and A. S. Rajawat from SAC are acknowledged for their support. We extend our thanks to all observatory staffs of IIG for their support and collection of cGPS data. Figures were prepared using GMT software (http://gmt.soest.hawaii.edu/). We thank the anonymous reviewers, Mikael Attal (Associate Editor), and Noah Finnegan (Editor) for providing the constructive suggestions.

References

Ader, T., Avouac, J.-P., Liu-Zeng, J., Lyon-Caen, H., Bollinger, L., Galetzka, J., et al. (2012). Convergence rate across the Nepal Himalaya and interseismic coupling on the Main Himalayan Thrust: Implications for seismic hazard. *Journal of Geophysical Research*, *117*(B4), B04403. https://doi.org/10.1029/2011JB009071

Agnew, D. (1997). NLOADF: A program to for computing ocean-tide loading. *Journal of Geophysical Research*, *102*(B3), 5109–5110. https://doi.org/10.1029/96JB03458

Altamimi, Z., Collilieux, X., & Metivier, L. (2011). ITRF2008: An improved solution of the International Terrestrial Reference Frame. *Journal of Geodesy*, *85*(8), 457–473. https://doi.org/10.1007/s00190-011-0444-4

Amos, C. B., Audet, P., Hammond, W. C., Burgmann, R., Johanson, I. A., & Blewitt, G. (2014). Uplift and seismicity driven groundwater depletion in central California. *Nature*. https://doi.org/10.1038/nature13275

Bettinelli, P., Avouac, J. P., Flouzat, M., Bollinger, L., Ramillien, G., Rajaure, S., & Sapkota, S. (2008). Seasonal variations of seismicity and geodetic strain in the Himalaya induced by surface hydrology, Earth Planet. *Science Letters*, *266*(3-4), 332–344. https://doi.org/10.1016/j.epsl.2007.11.021

Bilham, R., Larson, K., & Freymueller, J. (1997). GPS measurements of present-day convergence across the Nepal Himalaya. *Nature*, *386*, 61–64.

Bilham, R., Mencin, D., Bendik, R., & Bürgmann, R. (2017). Implications for elastic energy storage in the Himalaya from the Gorkha 2015 earthquakes and other incomplete ruptures of the Main Himalayan Thrust. *Quaternary International*, *462*, 3–21. https://doi.org/10.1016/j.quaint.2016.09.055

Blewitt, G., & Lavallée, D. (2002). Effect of annual signals on geodetic velocity. *Journal of Geophysical Research*, *107*(B7), ETG 9-1–ETG 9-11. https://doi.org/10.1029/2001JB000570

Bohem, J., Werl, B., & Schuh, H. (2006). Troposphere mapping functions for GPS and very long baseline interferometry from European Centre for Medium-Range weather forecasts operational analysis data. *Journal of Geophysical Research - Solid Earth*, *111*(B2), B2406.

Bookhagen, B., & Burbank, D. W. (2010). Toward a complete Himalayan hydrological budget: Spatiotemporal distribution of snowmelt and rainfall and their impact on river discharge. *Journal of Geophysical Research*, *115*(F3), F03019. https://doi.org/10.1029/2009JF001426

Chanard, K., Avouac, J. P., Ramillien, G., & Genrich, J. (2014). Modeling deformation induced by seasonal variations of continental water in the Himalaya region: Sensitivity to Earth elastic structure. *Journal of Geophysical Research - Solid Earth*, *119*(6), 5097–5113. https://doi.org/10.1002/2013JB010451

Chen, J. L., Wilson, C. R., Li, J., & Zhang, Z. Z. (2015). Reducing leakage error in GRACE-observed long-term ice mass change: A case study in West Antarctica. *Journal of Geodesy*, *89*(9), 925–940. https://doi.org/10.1007/s00190-015-0824-2

Davis, J. L., Elósegui, P., Mitrovica, J. X., & Tamisiea, M. E. (2004). Climate-driven deformation of the solid Earth from GRACE and GPS. *Geophysical Research Letters*, *31*(24), L24605. https://doi.org/10.1029/2004GL021435

Farrell, W. E. (1972). Deformation of the Earth by surface loads. *Reviews of Geophysics*, *10*(3), 761–797. https://doi.org/10.1029/RG010i003p00761

Fu, Y., & Freymueller, J. T. (2012). Seasonal and long-term vertical deformation in the Nepal Himalaya constrained by GPS and GRACE measurements. *Journal of Geophysical Research*, *117*(B3), B03407. https://doi.org/10.1029/2011JB008925

Fu, Y., Freymueller, J. T., & Jensen, T. (2012). Seasonal hydrological loading in southern Alaska observed by GPS and GRACE. *Geophysical Research Letters*, *39*(15), L15310. https://doi.org/10.1029/2012GL052453

Gautam, P. K., Gahalaut, V. K., Prajapati, S. K., Kumar, N., Yadav, R. K., Rana, N., & Dabral, C. P. (2017). Continuous GPS measurements of crustal deformation in Garhwal- Kumaun Himalaya. *Quaternary International*, *462*, 124–129,ISSN 1040-6182. https://doi.org/10.1016/j.quaint.2017.05.043

Hao, M., Freymueller, J. T., Wang, Q., Cui, D., & Qin, S. (2016). Vertical crustal movement around the southeastern Tibetan Plateau constrained by GPS and GRACE data, Earth Planet. *Science Letters*, *437*, 1–8.

He, M., Shen, W., Pan, Y., Chen, R., Ding, H., & Guo, G. (2018). Temporal–spatial surface seasonal mass changes and vertical crustal deformation in South China Block from GPS and GRACE measurements. *Sensors*, *18*, 99.

Herring, T. (2003). MATLAB Tools for viewing GPS velocities and time series. *GPS Solutions*, *7*(3), 194–199. https://doi.org/10.1007/s10291-003-0068-0

Herring, T.A., (2005), GLOBK, Global Kalman filter VLBI and GPS analysis program, Version 10.2, Report, Department of Earth, Atmospheric and Planetary Sciences, Massachussetts Institute of Technology.

Jade, S., Mukul, M., Gaur, V. K., Kumar, K., Shrungeshwar, T. S., Styal, G. S., et al. (2014). Contemporary deformation in the Kashmir-Himachal, Garhwal nd Kumaon Himalaya: significant insights from 1995-2008 GPS time series. *Journal of Geodesy*, *88*(6), 539–557. https://doi.org/10.1007/s00190-014-0702-3

Jin, S. G., Van Dam, T., & Wdowinski, S. (2013). Observing and understanding the Earth system variations from space geodesy. *Journal of Geodynamics*, *72*, 1–10. https://doi.org/10.1016/j.jog.2013.08.00

Johnson, C. W., Fu, Y. N., & Burgmann, R. (2017). Seasonal water storage, stress modulation, and California seismicity. *Science*, *356*(6343), 1161–1164. https://doi.org/10.1126/science.aak9547

King, M. A., & Watson, C. S. (2014). Geodetic vertical velocities affected by recent rapid changes in polar motion. *Geophysical Journal International*, *199*(2), 1161–1165. https://doi.org/10.1093/gji/ggu325

King, R.W., & Bock, Y. (2005). Documentation of the GAMIT GPS Analysis Software, Massachusetts Institute of Technology.

Krystek, M., & Anton, M. (2007). A weighted total least-squares algorithm for fitting a straight line. *Measurement Science and Technology*, *18*(11), 3438–3442. https://doi.org/10.1088/0957-0233/18/11/025

Kundu, B., Vissa, N. K., & Gahalaut, V. K. (2015). Influence of anthropogenic groundwater unloading in Indo-Gangetic plains on the 25 April 2015 *Mw* 7.8 Gorkha, Nepal earthquake. *Geophysical Research Letters*, *42*(24), 10,607–10,613. https://doi.org/10.1002/2015GL066616

Lavé, J., & Avouac, P. (2000). Active folding of fluvial terraces across the Siwalik Hills, Himalayas of central Nepal. *Journal of Geophysical Research*, *105*(B3), 5735–5770. https://doi.org/10.1029/1999JB900292

Lemoine, J.-M., Bruinsma, S., Gégout, P., Biancale, R., & Bourgogle, S. (2013). Release 3 of the GRACE gravity solutions from CNES/CRGS. Geophysical Research Abstracts, 15, EGU2013-11123, 2013.

Matsuo, K., & Heki, K. (2010). Time-variable ice loss in Asian high mountains from satellite gravimetry, Earth Planet. *Science Letters*, *290*(1-2), 30–36. https://doi.org/10.1016/j.epsl.2009.11.053

Mishra, S. K., Singh, R. P., & Chandra, S. (1993). Prediction of subsidence in Indo-Gangetic basin carried by groundwater withdrawal. *Engineering Geology*, *33*(3), 227–239. https://doi.org/10.1016/0013-7952(93)90060-P

Molnar, P. (1990). A review of the seismicity and the rates of active underthrusting and deformation at the Himalaya. *Journal of Himalayan Geology*, *1*, 131–154.
Molnar, P., & Tapponnier, P. (1975). Cenozoic tectonics of Asia: Effects of a continental collision. *Science*, *189*(4201), 419–426. https://doi.org/10.1126/science.189.4201.419
Nikolaidis, R. (2002), Observation of geodetic and seismic deformation with the Global Positioning System, Ph.D. thesis, Univ. of Calif., San Diego, San Diego.
Pagiatakis, S. D. (1990). The response of a realistic earth to ocean tide loading. *Geophysical Journal International*, *103*(2, 1 November, Pages), 541–560. https://doi.org/10.1111/j.1365-246X.1990.tb01790.x
Pan, Y., Shen, W.-B., Shum, C. K., & Chen, R. (2018). Spatially varying surface seasonal oscillations and 3-D crustal deformation of the Tibetan Plateau derived from GPS and GRACE data. *Earth and Planetary Science Letters*, *502*, 12–22, ISSN 0012-821X. https://doi.org/10.1016/j.epsl.2018.08.037
Panda, D., Kundu, B., Gahalaut, V. K., Bürgmann, R., Jha, B., Asaithambi, R., et al. (2018). Seasonal modulation of deep slow-slip and earthquakes on the Main Himalayan Thrust. *Nature Communications*, *9*(1), 1–8. https://doi.org/10.1038/s41467-018-06371-2
Rodell, M., Velicogna, I., & Famiglietti, J. S. (2009). Satellite-based estimates of groundwater depletion in India. *Nature*, *460*(7258), 999–1002. https://doi.org/10.1038/nature08238
Singh, S. J., & Rani, S. (1993). Crustal deformation associated with two dimensional thrust faulting. *Journal of Physics of the Earth*, *41*(2), 87–101. https://doi.org/10.4294/jpe1952.41.87
Steckler, M. S., Nooner, S. L., Akhter, S. H., Chowdhury, S. K., Bettadpur, S., Seeber, L., & Kogan, M. G. (2010). Modeling Earthdeformation from monsoonal flooding in Bangladesh using hydrographic, GPS, andGravity Recovery and Climate Experiment (GRACE) data. *Journal of Geophysical Research*, *115*, B08407. https://doi.org/10.1029/2009JB007018
Sreejith, K. M., Sunil, P. S., Agrawal, R., Saji, A. P., Ramesh, D. S., & Rajawat, A. S. (2016). Coseismic and early postseismic deformation due to the 25 April 2015, *Mw* 7.8 Gorkha, Nepal, earthquake from InSAR and GPS measurements. *Geophysical Research Letters*, *43*(7), 3160–3168. https://doi.org/10.1002/2016GL067907
Sreejith, K. M., Sunil, P. S., Agrawal, R., Saji, A. P., Ramesh, D. S., & Rajawat, A. S. (2018). Audit of stored strain energy and extent of future earthquake rupture in central Himalaya. *Scientific Reports*, *8*(1), 16697. https://doi.org/10.1038/s41598-018-35025-y
Swenson, S., Chambers, D., & Wahr, J. (2008). Estimating geocenter variations from a combination of GRACE and ocean model output. *Journal of Geophysical Research - Solid Earth*, *113*, B8.
Swenson, S., & Wahr, J. (2006). Post-processing removal of correlated errors in GRACE data. *Geophysical Research Letters*, *33*, L08402. https://doi.org/10.1029/2005GL025285
Tapley, B. D., Bettadpur, S., Ries, J. C., Thompson, P. F., & Watkins, M. M. (2004). GRACE measurements of mass variability in the Earth System. *Science*, *305*(5683), 503–505. https://doi.org/10.1126/science.1099192
Tesmer, V., Steigenberger, P., van Dam, T., & Mayer-Gürr, T. (2011). Vertical deformations from homogeneously processed GRACE and global GPS long-term series. *Journal of Geodesy*, *85*(5), 291–310. https://doi.org/10.1007/s00190-010-0437-8
Tian, Y. (2011). iGPS: IDL tool package for GPS position time series analysis. *GPS Solutions*, *15*(3), 299–303. https://doi.org/10.1007/s10291-011-0219-7
Tiwari, V. M., Srinivas, N., & Singh, B. (2014). Hydrological changes and vertical crustal deformation in south India: Inference from GRACE GPS and absolute gravity data. *Physics of the Earth and Planetary Interiors*, *231*, 74–80. https://doi.org/10.1016/j.pepi.2014.03.002
Tiwari, V. M., Wahr, J., & Swenson, S. (2009). Dwindling groundwater resources in northern India, from satellite gravityobservations. *Geophysical Research Letters*, *36*, L18401. https://doi.org/10.1029/2009GL039401
Tregoning, P., & van Dam, T. (2005). Atmospheric pressure loading corrections applied to GPS data at the observation level. *Geophysical Research Letters*, *32*(22), L22310. https://doi.org/10.1029/2005GL024104
Tregoning, P., Watson, C., Ramillien, G., McQueen, H., & Zhang, J. (2009). Detecting hydrologic deformation using GRACE and GPS. *Geophysical Research Letters*, *36*(15), L15401. https://doi.org/10.1029/2009GL038718
van Dam, T. (2010). NCEP derived 6 hourly, global surface displacements at 2.5 × 2.5 degree spacing. [Available at http://geophy.uni.lu/ncep-loading.html.]
van Dam, T., Collilieux, X., Wuite, J., Altamimi, Z., & Ray, J. (2012). Nontidal ocean loading effects in GPS height time series. *Journal of Geodynamics*, *86*(11), 1043–1057. https://doi.org/10.1007/s00190-012-0564-5
van Dam, T., Wahr, J., & Lavallee, D. (2007). A comparison of annual vertical crustal displacements from GPS and Gravity Recovery and Climate Experiment (GRACE) over Europe. *Journal of Geophysical Research*, *112*(B3), B03404. https://doi.org/10.1029/2006JB004335
van Dam, T. M., Blewitt, G., & Heflin, M. B. (1994). Atmospheric pressure loading effects on Global Positioning System coordinate determinations. *Journal of Geophysical Research*, *99*(B12), 23939–23950. https://doi.org/10.1029/94JB02122
van Dam, T. M., & Wahr, J. M. (1987). Displacements of the Earth's surface due to atmospheric loading: Effects on gravity and baseline measurements. *Journal of Geophysical Research*, *92*(B2), 1281–1286. https://doi.org/10.1029/JB092iB02p01281
Wahr, J., Molenaar, M., & Bryan, F. (1998). Time variability of the Earth's gravity field: Hydrological and oceanic effects and their possible detection using GRACE. *Journal of Geophysical Research*, *103*(B12), 30205–30229. https://doi.org/10.1029/98JB02844
Wdowinski, S., Bock, Y., Zhang, J., Fang, P., & Genrich, J. (1997). Southern California permanent GPS geodetic array: Spatial filtering of daily positions for estimating coseismic and postseismic displacements induced by the 1992 Landers earthquake. *Journal of Geophysical Research*, *102*(B8), 18057–18070. https://doi.org/10.1029/97JB01378
Williams, S. D. P., & Penna, N. T. (2011). Non-tidal ocean loading effects on geodetic GPS heights. *Geophysical Research Letters*, *38*(9), L09314. https://doi.org/10.1029/2011GL046940
Zhao, W., Kumar, P., Mechie, J., Kind, R., Meissner, R., Wu, Z., et al. (2011). Tibetan plate overriding the Asian plate in central and northern Tibet. *Nature Geoscience*, *4*(12), 870–873. https://doi.org/10.1038/NGEO1309
Zou, R., Wang, Q., Freymueller, J., Poutanen, M., Cao, X. L., Zhang, C. H., et al. (2015). Seasonal hydrological loading in southern Tibet detected by joint analysis of GPS and GRACE. *Sensors*, *15*(12), 30525–30538. https://doi.org/10.3390/s151229815